






Electrostatic actuators with constant force at low power loss using matched dielectrics

Received: 7 September 2023

Accepted: 4 October 2023

Published online: 09 November 2023

 Check for updates


Ion-Dan Sirbu ^{1,2,3,6}, David Preninger ^{4,5,6}, Doris Danninger ^{4,5},
Lukas Penkner^{4,5}, Reinhard Schwödiauer^{4,5}, Giacomo Moretti ¹,
Nikita Arnold ^{4,5}, Marco Fontana ^{2,3}  & Martin Kaltenbrunner ^{4,5} 

Electrostatic multilayer systems, which often employ thin polymer films in combination with displaceable insulating fluids, can enable actuation in applications such as soft robotics. Driven by high electric fields, they provide strong performance in terms of power density, actuation strain and speed, but suffer from rapid force decay due to interfacial charging. High-frequency polarity inversion of driving voltages is a remedy, but involves large power consumption and unfavourable force oscillations. Here we report a theoretical and experimental framework for the force behaviour in generic solid/liquid-dielectric multilayer stacks independent of actuator design and solely based on their dielectric properties. We use this model to develop materials-based solutions, which rely on matching the bulk charge relaxation rates of the constituent dielectrics, for a variety of soft actuator systems: tunable lenses, artificial muscles and haptic devices. The approach provides indefinite, steady force output under constant-voltage operation, with up to 1,000-fold power loss reduction compared with unmatched material combinations.

Robotic devices based on soft materials can provide compatibility with living organisms^{1–4} and a range of functions^{5–8}, as well as operate in demanding terrains and across various scales. Yet, they are typically manufactured from polymers^{4,9,10} at potentially low production costs¹¹. They actuate under diverse stimuli, including heat, light or chemical cues^{12–14}, magnetic or electric fields^{15–17} and fluid pressure variations^{1,3}. Each system can excel in specific actuation parameters, but is highly limited in other aspects. For instance, thermo-responsive polymers can offer high work densities (over 2 kJ kg^{-1})^{18,19} or large strains (200%)²⁰, but are confined to low actuation frequencies. Photostrictive and magnetically driven robots thrive in wireless applications but require transparent media¹⁵ or inefficient field generators⁶. Electroactive polymer-based systems lend themselves to numerous topologies and operate over broad frequency ranges, but their force density is limited by the elastomer stiffness¹⁷. Fluidic-driven solutions reach large power densities, but require bulky and expensive pumps and storage systems¹.

Electrostatic multilayered systems (EMSs), which combine the principles of dielectric elastomer transducers (a type of high-strain electrostatic actuators) with pressure-induced deformations of fluidic actuation systems, offer a versatile technology with self-sensing^{21,22} and self-healing²³ capabilities. EMSs actuate due to Coulomb attraction between electrodes and deform, stretch and/or displace (often through a zipping mechanism) some of the fluid dielectrics in multilayer stacks²⁴. They are the foundation for contractile artificial muscles^{25–29}, grippers³⁰ and soft tunable optical systems³¹. This technology is also employed in wearable devices for haptic feedback^{32–34}, airborne robots³⁵ and energy harvesters^{29,36}.

However, charge accumulation at the interfaces between different dielectrics alters the electric field within the stack, leading to a fast decay of the force output. EMSs are, thus, incapable of static actuation when subject to direct-current (d.c.) high voltage, which limits their applicability. The current widespread remedy is to use

¹Department of Industrial Engineering, University of Trento, Trento, Italy. ²Department of Excellence of Robotics and AI, Scuola Superiore Sant'Anna, Pisa, Italy. ³Institute of Mechanical Intelligence, Scuola Superiore Sant'Anna, Pisa, Italy. ⁴Division of Soft Matter Physics, Institute for Experimental Physics, Johannes Kepler University, Linz, Austria. ⁵Soft Materials Lab, Linz Institute of Technology, Johannes Kepler University, Linz, Austria. ⁶These authors contributed equally: Ion-Dan Sirbu, David Preninger.  e-mail: marco.fontana@santannapisa.it; martin.kaltenbrunner@jku.at

alternating-current (a.c.) square-wave high-voltage signals with high duty cycles and frequencies of 50–200 Hz (ref. 32). This, though, can only be achieved with complex power electronics. The fast polarity switching is intended to cyclically redistribute the charges and achieve nearly constant forces, at the expense of high energetic losses and the generation of force oscillations that are particularly detrimental to high-precision applications. The typical high operating voltages may limit applications within sensitive environments.

In this article, we report a theoretical and experimental framework that captures the underlying physical processes—and the resulting force responses—in EMSs. Our model analyses and forecasts system behaviour solely based on the parameters of the dielectrics employed: conductivity, permittivity and thicknesses. We first experimentally verify our theoretical predictions using a purpose-built force measurement system, which allows for the rapid screening of material combinations independent of a specific actuator design. We show that established dielectric material combinations of polymer films and insulating oils exhibit the predicted force decay, illustrating the limitations of existing approaches for quasistatic actuation.

Our framework also provides a solution for achieving indefinite, constant-force output with a d.c. high voltage: matching the bulk charge relaxation rates of the constituting dielectrics, thereby preventing detrimental charge accumulation. This is achieved by replacing the commonly used polymer films with less-insulating ones, yielding a constant-force output despite being driven by a d.c. voltage. Suitable films include a polyester-based dielectric and an ultrathin relaxor ferroelectric terpolymer that unlocks operating voltages below 1,000 V. Simultaneously, matched dielectrics can cut the power loss density by up to three orders of magnitude compared with conventional approaches. We illustrate the universality of our method by achieving steady-state actuation (that is, void of electrode unzipping) in a range of EMSs: zipping electroactive polymer (ZEAP) lenses³¹, soft hydraulically amplified taxels (HAXELs)³², electrostatic bellow muscles (EBMs)²⁹ and Peano-hydraulically amplified self-healing electrostatic (HASEL)²⁶ actuators.

Theoretical framework

Typical EMS designs comprise two flexible or stretchable dielectric films coated with electrodes that enclose a displaceable fluid dielectric^{26,29,31}. On application of a suitably high voltage, Coulomb attraction deforms the globally soft system. Specialized actuator geometries yield artificial muscles, tunable optics, haptics and many other applications (Fig. 1a).

The minimal model of an EMS contains two planar layers: a liquid dielectric of thickness t_L and a polymeric dielectric film of thickness t_F with the relative permittivities and electric conductivities of ϵ_L, σ_L and ϵ_F, σ_F , respectively (Fig. 1b). Although the actual composition and number of layers in real systems might be more complex, this system provides a broad insight into the electrical dynamics of EMSs. Supplementary Information provides the generalizations and mathematical details. In particular, the ‘Frequency-domain analysis’ section in Supplementary Information shows that all layers of the same material can be described as one with the combined thickness. Furthermore, it extends the materials-matching concept to arbitrary non-planar shapes. The ‘Relaxation times and steady state for multimaterial systems’ section in Supplementary Information provides guidelines to model stacks with three and more materials.

As all dielectrics are non-ideal insulators, small unequal currents flow through all layers when voltage U is applied; their densities are j_L and j_F in the liquid and film, respectively, and $j_M = j_M$ in the respective adjacent metal electrodes (Supplementary Equation (23)). The dielectric current densities depend on the corresponding conductivities and the local electric fields E_L and E_F . No volume (space) charges are present, but following a voltage step, surface charges are formed and subsequently modified at all interfaces. Their densities are ρ_L and ρ_F

at the dielectric–electrode contacts, and ρ_{FL} at the interface between the dielectrics (Supplementary Equation (11)). The system dynamics is mainly determined by ρ_{FL} , which changes from zero to a stationary value ρ_∞ with the system time constant τ (Supplementary Equations (15) and (16)). This charge redistribution alters the fields (Supplementary Equation (14)), which determine the actuation forces and electrical breakdown (Supplementary Equation (19)). Related charge accumulation effects are known as Maxwell–Wagner–Sillars polarization^{37–43}. The attractive force F between the electrodes of an area S (Supplementary Fig. 1) is given by the Maxwell stress p_L within the liquid (Supplementary Equations (24)–(26)). Its temporal behaviour is determined by the square of the liquid field E_L (Supplementary Equations (19)). The single-exponential dynamics of the field can be extracted from the square root of the force using log-ordinate (on shifting).

$$\sqrt{F} = \sqrt{F_\infty} + (\sqrt{F_0} - \sqrt{F_\infty})e^{-t/\tau} \quad (1)$$

Equation (1) contains the starting and steady-state forces F_0 and F_∞ , respectively, and time constant τ (derived in Supplementary Equations (15) and (27)).

$$F_0 = \frac{\epsilon_L}{8\pi} \left(\frac{U}{t_L + t_F \epsilon_L / \epsilon_F} \right)^2 S, \quad (2)$$

$$F_\infty = \frac{\epsilon_L}{8\pi} \left(\frac{U}{t_L + t_F \sigma_L / \sigma_F} \right)^2 S, \quad \tau = \frac{1}{4\pi} \frac{\epsilon_L t_F + \epsilon_F t_L}{\sigma_L t_F + \sigma_F t_L}$$

Equations (1) and (2) show how the force dynamics depends on the layer thicknesses and material properties (Fig. 1c). In the initial ‘electrostatic’ response F_0 at time $t = 0$, the interfacial charge $\rho_{FL} = 0$, whereas the fields (Supplementary Equation (19)) depend only on the dielectric constants (like in an instantly charged ideal capacitor). For F_∞ at $t \rightarrow \infty$, the interfacial charge density stabilizes at $\rho_{FL} \rightarrow \rho_\infty$, whereas the final fields $E_{L,\infty}$ and $E_{F,\infty}$ (Supplementary Equation (19)) equalize the stationary currents $j_F = j_L = j_\infty$ in both layers (Supplementary Equation (17)) and electrodes (Supplementary Equation (23)) and therefore depend only on the conductivities. Charge relaxation time constants of bulk materials τ_F and τ_L (Supplementary Equations (8) and (9)) provide a simple expression for ρ_∞ , illustrating that no interfacial charge forms when they match.

$$\tau_F = \frac{\epsilon_F}{4\pi\sigma_F}, \quad \tau_L = \frac{\epsilon_L}{4\pi\sigma_L} \rightarrow \rho_\infty = (\tau_F - \tau_L)j_\infty \quad (3)$$

The variation in attractive force F is related to the change in liquid field $E_{L,\infty}/E_{L,0}$ (Supplementary Equations (20) and (28)). In the zipped state, where the liquid is vanishingly thin, this field change reduces to the ratio of the material relaxation times.

$$t_L \ll t_F \rightarrow \frac{E_{L,\infty}}{E_{L,0}} \approx \frac{\tau_L}{\tau_F} \quad (4)$$

Equations (3) and (4) with the given material parameters $\epsilon_{F/L}, \sigma_{F/L}$ predict three possible force responses for zipped systems with $t_L \ll t_F$ (and even in general, as shown in Supplementary Equation (20)): (1) $F_\infty < F_0$ for $\tau_F > \tau_L$; (2) $F_\infty > F_0$ for $\tau_F < \tau_L$; (3) $F_\infty \approx F_0$ when $\tau_F \approx \tau_L$. Case (3) maintains the initial force unchanged; cases (1) and (2) also ultimately result in a force plateau—but at different levels than F_0 . For common material combinations used in EMSs so far (case (1)), the steady-state zipping force will stabilize near zero. The mechanism of the actuator force decay is explained in the ‘Unzipping pressure and the deterioration of the actuator force and stroke’ section in Supplementary Information using the example of Peano-HASEL⁴⁴ (Supplementary Fig. 2). Our framework resolves this issue as it permits a precise adjustment of the output force via a selection of films or fluids with proper conductivities or permittivities. EMSs can, therefore, maintain or even increase

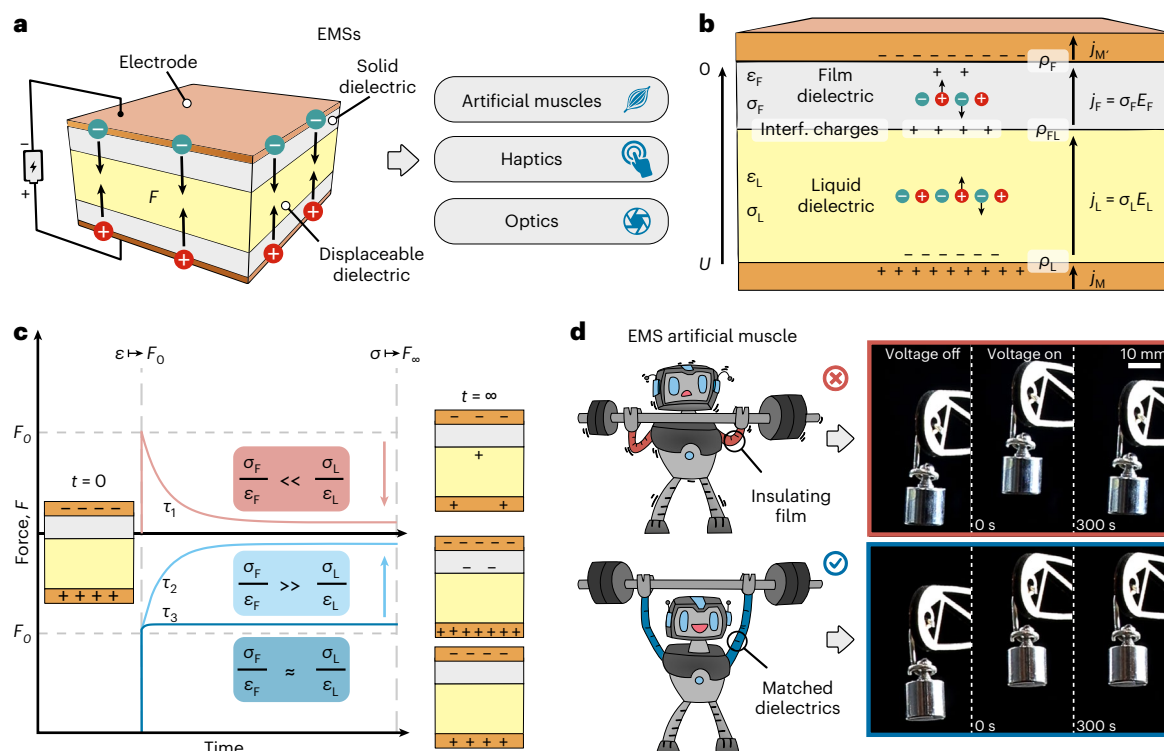


Fig. 1 | Soft EMSs. **a**, Electrostatic force F between the charges on the electrodes (orange) insulated by the polymer films (grey) squeezes a displaceable dielectric (for example, liquid oil; yellow). This is used for various applications (examples listed on the right). **b**, Charge dynamics. The sequence of arrows indicates the magnitudes of current densities j in all the materials. Larger leakage through the liquid accumulates charge (density) ρ_{FL} at the central interface; fields and electrode charges ρ_L and ρ_F also modify until all the currents equalize. **c**, Resulting force changes. The initial force F_0 is predominantly determined by the dielectric permittivity ϵ . The force stabilizes towards the conductivity-based value F_∞ with

the system time constant τ . F_∞ is much lower than F_0 when the film has a slower bulk relaxation rate ($\ll \sigma/\epsilon$) than the liquid (red). For matched material relaxation (blue), the force stays constant, or even increases, if the film is more conducting (light blue). The initial charges (left inset) redistribute into three different final states, shown near the ends of the respective curves. **d**, Artificial muscles with an insulating film (or lossy liquid) lose tension and drop the weight (top-right panel, red), whereas for the matched dielectrics below, the force persists (blue) when driving a robotic end effector.

their initial force when driven by d.c. high-voltage signals instead of losing tension. We experimentally demonstrated this behaviour with a contractile EMS muscle unable to hold a payload when fabricated from conventional materials, but steadily supporting the weight when matched dielectrics were used (Fig. 1d). Once the problem of force relaxation is resolved, various specific actuators can be described in the lowest order along the lines of energy balance, such as those used in previous works^{29,31,44}. Viscous effects are neglected in our quasistatic analysis targeting a constant-force output; they become relevant for fast actuation⁴⁵.

Force measurements

We verify this theoretical model against electrostatic forces in a multi-layer dielectric stack (functioning as a generic EMS), measured with a custom optomechanical test bench (Fig. 2a and Supplementary Fig. 3). This stack consisted of three dielectric layers: two polymer films with an aggregated thickness of 48–66 μm and a 1-mm-thick unpressurized oil layer (Supplementary Fig. 4). The dielectrics were enclosed by two electrodes—one movable and attached to the tip of a cantilever (Extended Data Fig. 1) and the other one, fixed. First, we investigated biaxially oriented polypropylene (BOPP), polyimide (PI), polyethylene terephthalate (PET) and polyvinylidene fluoride (PVDF), common dielectric films with measured σ_F ranging from 10^{-16} to 10^{-13} S m^{-1} and ϵ_F between 2.40 and 14.38, in combination with FR3 oil ($\sigma_L = 6 \times 10^{-12}$ S m^{-1} and $\epsilon_L = 3.20$; Supplementary Tables 1 and 2).

On application of a constant high-voltage signal (8 kV for 600 s), the initial force F_0 decreases rapidly (Fig. 2b). This temporal behaviour

is characterized by the system time constant τ in equation (1). The stacks containing PET, BOPP and PI have time constants ranging from 70 to 115 s and final forces $F_\infty \approx 0$ mN. PVDF exhibits a τ value of 350 s and a decreasing force that settles at ~ 12 mN after 600 s, roughly 27% of F_0 . The larger τ is mainly due to PVDF's larger permittivity, whereas the higher F_∞ is due to higher conductivity.

Charges accumulated at the solid/liquid-dielectric interfaces create a residual electric field that results in another force spike after the voltage is turned off, which is also reflected in our theoretical discussion (Supplementary Equation (29)).

We present a route for maintaining the zipping force constant or even increasing it by replacing the highly insulating films with one with higher conductivity to yield appropriate dielectric properties, $\sigma_F/\epsilon_F \geq \sigma_L/\epsilon_L$. Alternatively, dielectric liquids with at least three orders of magnitude lower conductivity than FR3 would match the highly insulating films ($\sigma_L \leq 10^{-15}$ S m^{-1} for $\epsilon_L \approx 3$; Supplementary Tables 1 and 2). However, such materials prove difficult to develop and are probably susceptible to environmental stressors (oxygen, water, impurities, ultraviolet radiation and so on) that diminish their insulating properties^{46,47}. Therefore, we investigated a 'lossy' biopolyester (BP) film, recently used for entirely biodegradable Peano-HASEL actuators⁴⁸. This material exhibits a conductivity of $\sigma_F = 2.8 \times 10^{-11}$ S m^{-1} and a permittivity of $\epsilon_F = 5$ (Supplementary Fig. 5).

BP yields an initial increase in force and a steady-state value $F_\infty > F_0$ about 30% larger than F_0 , since it has a shorter charge relaxation time than the oil: $\tau_F < \tau_L$. As a result, the measured system time constant also decreases towards $\tau \approx 10$ s.

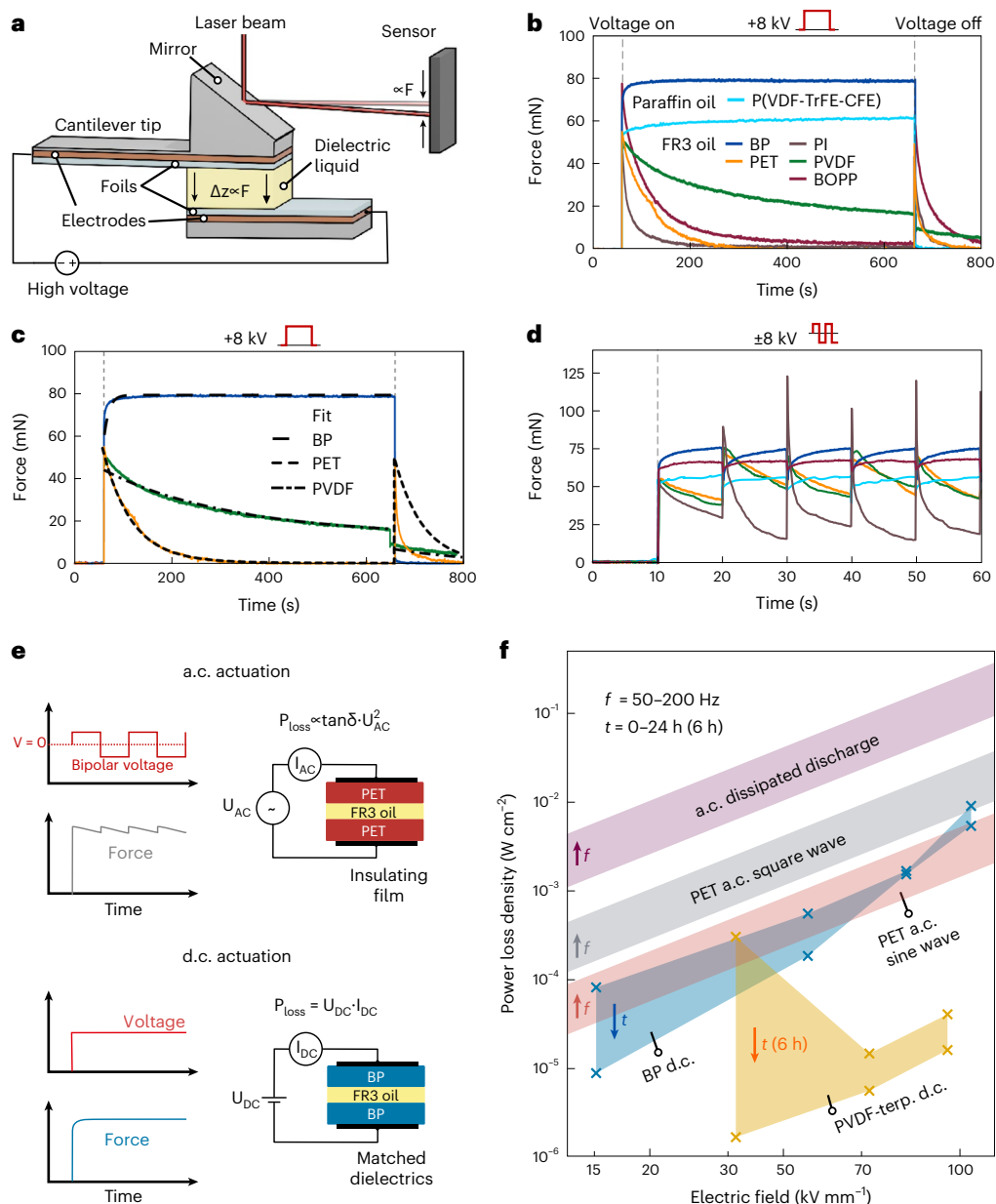


Fig. 2 | Force variation and power loss measurements in EMSs. **a**, Schematic of the force measurement principle. The electrostatic force between the electrodes, induced by the high voltage, bends the cantilever. Consequently, a laser beam is deflected via a mounted mirror, changing its spot position on the sensor. **b**, Measured force response to a high-voltage pulse with $U = 8$ kV and duration $\tau_{\text{pulse}} = 600$ s for six material combinations; all films are combined with FR3 oil except for P(VDF-TrFE-CFE) (paraffin oil). BP and the PVDF terpolymer—both lossy films—show a constant force, whereas other materials present decay with different relaxation times. **c**, Model validation on three of the materials presented in **b**. **d**, Force response of the six dielectric material combinations, as shown in

b, subject to a square-wave signal with 8 kV amplitude and $\tau_{\text{pulse}} = 20$ s. **e**, Two possible actuation modes and their respective methods of power consumption evaluation: with highly insulating dielectric films and more conductive dielectric fluid, driven by a square wave and leading to unstable actuation (top); with a dielectric liquid matched with lossy films, driven by a d.c. voltage, allowing smooth steady-state actuation (bottom). **f**, Power loss density as a function of electric field of P(VDF-TrFE-CFE), BP and PET films with thin layers of liquid dielectric in between, estimated from leakage current measurements (d.c. case) or dielectric spectroscopy (a.c. case).

Choosing a similarly conductive film with higher permittivity and/or lower thickness allows to substantially reduce the operational voltages. Therefore, as a second candidate, we employed an 8- μm -thick poly(vinylidene fluoride-trifluoroethylene-chlorofluoroethylene) (P(VDF-TrFE-CFE) or PVDF terpolymer) film. This relaxor ferroelectric polymer with a conductivity of $\sigma_f = 2.1 \times 10^{-11}$ and a permittivity of $\epsilon_f = 25.5$ has a nonlinear dielectric response at high field strengths, yet exhibits a narrow hysteresis, rendering it promising for electrostatic actuators (Supplementary Equation (36) and Supplementary Fig. 6).

In combination with paraffin oil ($\sigma_l = 2 \times 10^{-13}$ S m^{-1} and $\epsilon_l = 2.2$), the force increases: F_∞ is about 20% larger than F_0 .

The accuracy of our model can be proven by inserting F_0 , F_∞ and τ from the experiment (Supplementary Table 1) into equation (1) and comparing the resulting fits with the measured forces (Fig. 2c and Extended Data Fig. 2). Based on this, the dielectric properties of the materials can be further analysed, for example, τ deviations from the single-exponential behaviour (Extended Data Fig. 2a) and transient increase in force for poled BOPP (Fig. 2d and Extended Data Fig. 3e),

which imply more complex spectral dielectric properties like the Debye relaxation (Supplementary Information). However, our minimal theoretical framework with constant parameters already gives reliable estimates for system relaxation times τ , and predictions on the force transients solely using material properties (that is, $\epsilon_i, \sigma_i, t_i$).

Under square-wave excitation with an amplitude of 8 kV (Fig. 2d and Extended Data Figs. 3 and 4), the samples demonstrated a similar temporal behaviour as for the constant fields, apart from BOPP that can show two different trends (Extended Data Fig. 5). Pristine samples display immediate force decay after F_0 has been reached, like other highly insulating films. If BOPP has been previously subjected to high voltage, it displays an initial increase in force for up to 10 s (Fig. 2d), before decaying, which suggests poling-induced material alterations.

Furthermore, material combinations exhibiting interfacial charge accumulation display a stepwise increase in peak force (up to $4F_0$, for example, for PI and PET) when operated at a.c. voltages with low inversion frequencies. This allows for high pulsed forces at potentially low driving voltages (Supplementary Information and Supplementary Equation (30)).

As expected, the voltage dependence of force responses is approximately quadratic, that is, $F \propto U^2$ (Extended Data Fig. 6), with BP exhibiting high reproducibility (Extended Data Fig. 7).

Power losses for alternative EMS driving methods

To render d.c.-driven EMSs with matched dielectric stacks as an appealing solution, constant-force output and reduced energy usage must be simultaneously achieved (Fig. 2e). The state-of-the-art approach for constant-force output with highly insulating polymer films utilizes high-voltage high-duty-cycle bipolar square-wave driving. However, such stimuli require frequencies of up to 200 Hz to limit force fluctuations to acceptable levels³². Thus, it is important to identify the energetic losses associated with both methods.

We first investigate the complex frequency-dependent permittivity $\tilde{\epsilon}(\omega)$ of the stack, which is composed of a real part ϵ' , accounting for energy storage, and an imaginary part ϵ'' that accounts for losses. For some materials (for example, dielectric oils), the imaginary part ϵ'' is almost entirely ascribable to a real ohmic conductivity, that is, $\epsilon'' \approx 4\pi\sigma/\omega$. However, in polymer films, which are prone to complicated charge and field relaxation mechanisms⁴², ϵ''_F subdivides into the sum of a polarization contribution ϵ''_{pol} , and conductive losses, assuming that the latter are described by the second term in the last part of equation (5) with a real-valued conductivity σ_F .

$$\tilde{\epsilon}_F = \epsilon_F + i \frac{4\pi\sigma_F}{\omega} = \epsilon'_F + i\epsilon''_F, \quad \epsilon''_F = \epsilon''_{\text{pol}} + \frac{4\pi\sigma_F}{\omega} \quad (5)$$

Though both $\epsilon''_{\text{pol}}(\omega)$ and $\sigma_F(\omega)$ may still depend on angular frequency ω , for many of the polymeric materials used in this work, these parameters were found to weakly vary in the relevant range. Further extensions of equation (5) (including the dependencies of the material parameters on frequency) can be performed along the lines of the Debye model⁴², and can be understood in terms of auxiliary RC lumped elements (Supplementary Equation (86) and Supplementary Fig. 7). The power loss magnitude can be estimated by identifying which mechanism dominates ϵ'' in the considered frequency range (polarization or conductivity), and by identifying the relative contributions of the materials in the stack (Supplementary Equations (67)–(72)).

In the case of a harmonic excitation, the power loss in a zipped actuator (with $t_1 = 0$) stems from the polymer film (Supplementary Equation (68)) and is given by equation (6).

$$P = \frac{\omega \epsilon''_F S U^2}{8\pi t_F} = (\omega \epsilon''_{\text{pol}} + 4\pi\sigma_F) \frac{S U^2}{8\pi t_F} \mapsto \sigma_F \frac{S U^2}{t_F} \quad (6)$$

The second part of equation (6) separates polarization and conductivity contributions introduced in equation (5) and defines a.c. losses for highly insulating films, since at switching frequencies in the order of 10^2 Hz, the constant conductive part can be neglected. The last part of equation (6) refers to the losses for a d.c. voltage (leading to an additional factor of 2).

These equations elucidate the contributions of different mechanisms but are inconvenient for experimental analysis. To determine the real power loss values for both driving mechanisms, we use equivalent impedance-based expressions. Our samples consisted of two dielectric films with a dielectric liquid in between; the liquid thickness resembles the zipped state in EMSs (Fig. 2e). For d.c.-driven BP–FR3 oil and P(VDF-TrFE-CFE)–paraffin oil stacks, power losses can be extracted from voltage and current measurements, namely, $P_{\text{d.c.}} = U_{\text{d.c.}} I_{\text{d.c.}}$. However, the a.c.-driven PET–FR3 oil stacks involve frequency-dependent material parameters, that is, the dielectric loss factor $\tan\delta$ and the real part of the capacitance C' , obtained from dielectric spectroscopy. The power loss is calculated as $P_{\text{a.c.}} = \frac{1}{2} U_{\text{a.c.}}^2 C' \omega \tan\delta$ (Supplementary Equation (91)), where $U_{\text{a.c.}}$ is the amplitude of the a.c. signal.

The measured $\tan\delta$ of -0.007 and $C' \approx 21$ pF yield losses in the order of 10^{-4} W cm⁻² at 1 kV up to 10^{-2} W cm⁻² at 7 kV (Extended Data Fig. 8 and Supplementary Information). Since the power loss strongly depends on the actuation frequency, we calculate values for frequencies ranging from 50 to 200 Hz sinusoidal stimulus (bottom and top boundaries, respectively, in Fig. 2f (red-shaded area)). The voltage used for measuring $\tan\delta$ is relatively low (0.5 kV) compared with commonly used actuation amplitudes; hence, the estimated power loss may be regarded as conservative. A realistic high-voltage stimulus is expected to increase the loss factor and therefore also the corresponding power loss density. Additionally, the square-wave operation of EMSs will increase the power loss density fivefold compared with sinusoidal signals (Fig. 2f (grey-shaded area) and Supplementary Equations (75)–(79)). Furthermore, conventional high-voltage power supply circuits do not recycle the energy during the discharging phases of square-wave loading. The latter is drained on resistors and entirely lost at each polarity inversion. This leads to an additional contribution to the power loss $P_C = U^2 C' f$ for each polarity reversion (in addition to polarization losses), where f is the frequency (Fig. 2f, purple-shaded area).

The power loss for our matched dielectrics is two orders of magnitude (BP–FR3 oil) and three orders of magnitude (P(VDF-TrFE-CFE)–paraffin oil) smaller than the estimated a.c. power loss with dissipated discharge (Fig. 2f, blue-shaded area). We conducted leakage current measurements using consecutive high-voltage steps (Supplementary Fig. 8 and Extended Data Fig. 9), each applied for up to 24 h, with the top and bottom blue marks corresponding to the start and end of each step, respectively (Fig. 2f). Below a field strength of 60 kV mm⁻¹, the measured loss of BP is already lower than our conservative estimation for a.c. sinusoidal actuation and substantially lower (100 times) than the realistic a.c. power loss. Furthermore, for a field strength of up to 100 kV mm⁻¹, the measured loss of the PVDF terpolymer is up to two orders of magnitude lower than even the conservative estimate. Thus, fabricating EMSs with matching dielectrics and driving them with a d.c. voltage is considerably more energy efficient compared with previous approaches and prevents unwanted force oscillations.

Demonstrator prototypes

We demonstrate the capabilities of EMSs with matched dielectrics in several well-known zipping actuator layouts (Supplementary Table 3 lists the implemented materials). The zipping mechanism exploits the electrostatic forces between two opposing electrodes by progressively closing the gap in between, starting from points of closest distance. Two of these layouts utilize it to deform thin elastomeric membranes: the ZEAP lens³¹ (a soft tunable optical device) and the HAXEL (a wearable haptic actuator)³².

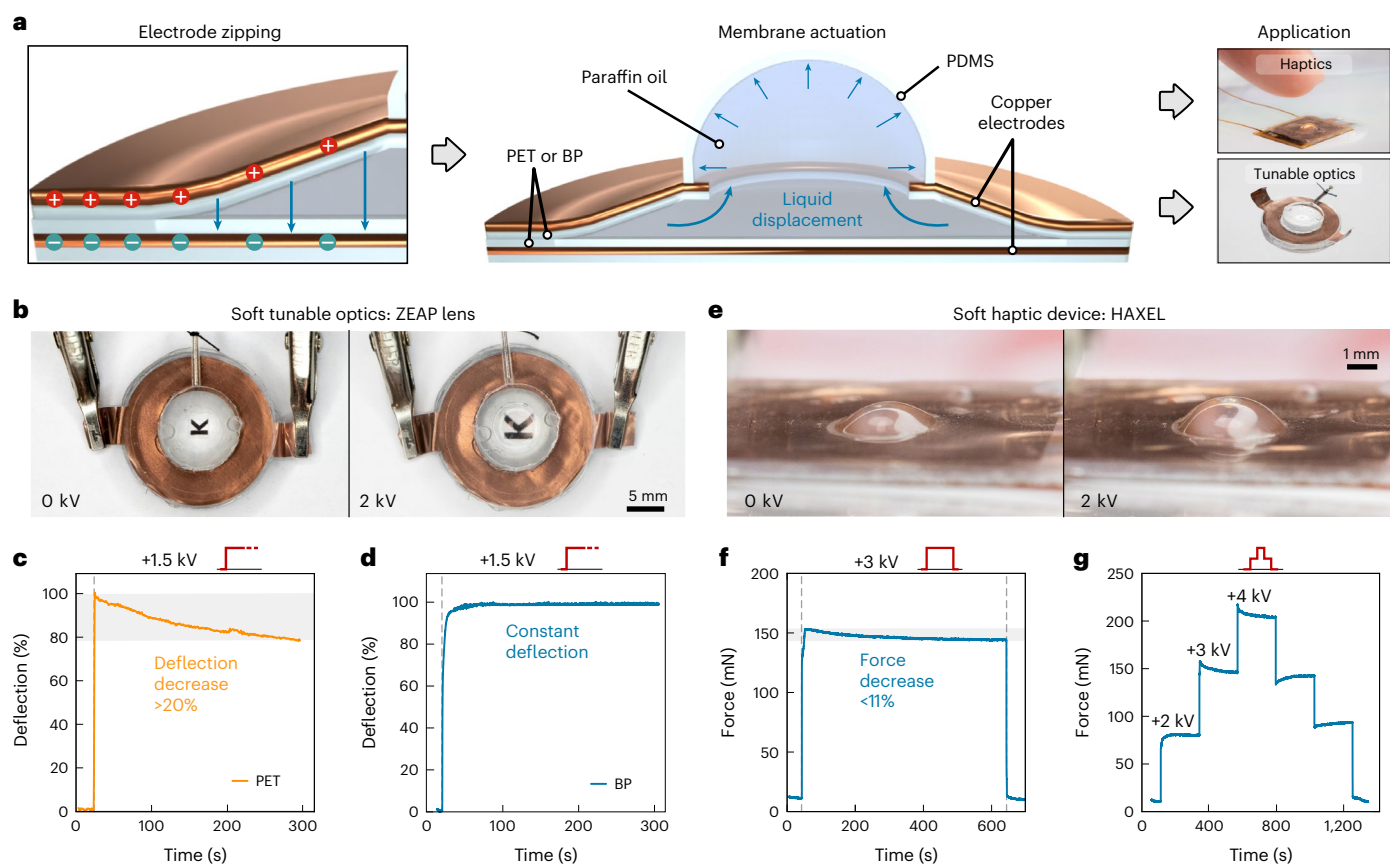


Fig. 3 | ZEAP lens and HAXEL actuators. **a**, Working principle. The electrostatic zipping of the electrode–polymer film bilayer leads to an increase in hydrostatic pressure in the dielectric fluid, that is, paraffin oil (Supplementary Table 2), and deform the membrane (Fig. 3a). In ZEAP lenses, this leads to changes in the focal length (Fig. 3b, Supplementary Video 1 and Supplementary Fig. 9). We evaluated their ability to maintain a constant focal length by tracking the deflection of a laser beam. A lens incorporating PET films exhibited a reduction in deflection of 20% from the initial value within 300 s when subjected to a d.c. high voltage (Fig. 3c). In contrast, a lens containing BP maintained the deflection for the same timeframe after an initial increase within the first ~30 s (Fig. 3d). This increase is due to the lower conductivity of the liquid compared with the BP film, as discussed in the previous sections. Under cyclic actuation, the lens exhibited repeatable and fast response (Supplementary Video 2).

Both devices zip BP or PET films to increase the hydrostatic pressure in the dielectric fluid, that is, paraffin oil (Supplementary Table 2), and deform the membrane (Fig. 3a). In ZEAP lenses, this leads to changes in the focal length (Fig. 3b, Supplementary Video 1 and Supplementary Fig. 9). We evaluated their ability to maintain a constant focal length by tracking the deflection of a laser beam. A lens incorporating PET films exhibited a reduction in deflection of 20% from the initial value within 300 s when subjected to a d.c. high voltage (Fig. 3c). In contrast, a lens containing BP maintained the deflection for the same timeframe after an initial increase within the first ~30 s (Fig. 3d). This increase is due to the lower conductivity of the liquid compared with the BP film, as discussed in the previous sections. Under cyclic actuation, the lens exhibited repeatable and fast response (Supplementary Video 2).

We also demonstrate the use of BP foil in a HAXEL (Fig. 3e and Supplementary Fig. 10), where the zipping mechanism and the resulting membrane deformation were used to generate haptic feedback. Subjecting the device to a 3 kV d.c. signal led to a constant-force output of 150 mN for more than 600 s, with less than 11% decrease (Fig. 3f) caused by stress relaxation in the membrane. In contrast, another work³² showed that HAXEL provides a constant-force output by using bipolar square-wave signals and frequencies above 150 Hz, although still presenting small force ripples. Our approach proves to be a viable alternative, entirely void of force oscillations. Finally, our device shows good controllability by stepwise variations in the voltage and thus the haptic feedback, enabling the indication of

the laser beam in the case of ZEAP lens with BP films subject to 1.5 kV d.c. signal. **e**, Relaxed state (left) and activated state (right) of a HAXEL actuator with BP and paraffin oil as the dielectrics and PDMS as the tactile membrane. **f**, HAXEL subject to a 3 kV high-voltage pulse, holding a force of around 150 mN for 600 s. The overall force relaxation is less than 11% and is due to mechanical relaxation in the system. **g**, Force output of the HAXEL under stepwise voltage variation.

different states or even communication mechanisms using one HAXEL (Fig. 3g).

Our approach of matching dielectrics can be additionally used in artificial muscles. Here we demonstrate the use of BP and P(VDF-TrFE-CFE) in a single-pouch EBM²⁹ and a four-pouch Peano-HASEL²⁶. Both devices were manufactured in multiple versions each: with either lossy or highly insulating polymer films, filled with respective dielectric liquids (Supplementary Table 3). The EBM had a circular pouch filled with a dielectric liquid, was radially constrained by thin stiffening rings and attached to a reservoir (Fig. 4a and Supplementary Fig. 11). The zipping of films results in the evacuation of the liquid dielectric into the reservoir, leading to a height change, termed stroke, of the muscle (Fig. 4b). After an initial contraction due to high-voltage (5 kV) activation, an EBM with PI films experienced a stroke decrease of around 95% in the first 5 s under 1 N load (Fig. 4c and Supplementary Video 3). On the contrary, an EBM made from BP, driven in the same conditions, demonstrated a 20% stroke increase within the first 30 s, after which it remained nearly constant at ~0.9 mm (Fig. 4d and Supplementary Video 4). Low-voltage steady-state actuation was shown in an EBM with P(VDF-TrFE-CFE) matched with paraffin oil dielectrics and mechanically enhanced by PI structural films (Methods). This device, at nearly 100% stroke, was able to hold a load of 0.1 N for 600 s while being driven by only 700 V d.c. (Fig. 4e). A comparable EBM with a PI dielectric and paraffin oil requires 2–3 kV to initially achieve 80–100% stroke (which then decays) under the same load. This higher voltage provides similar electrostatic energy density

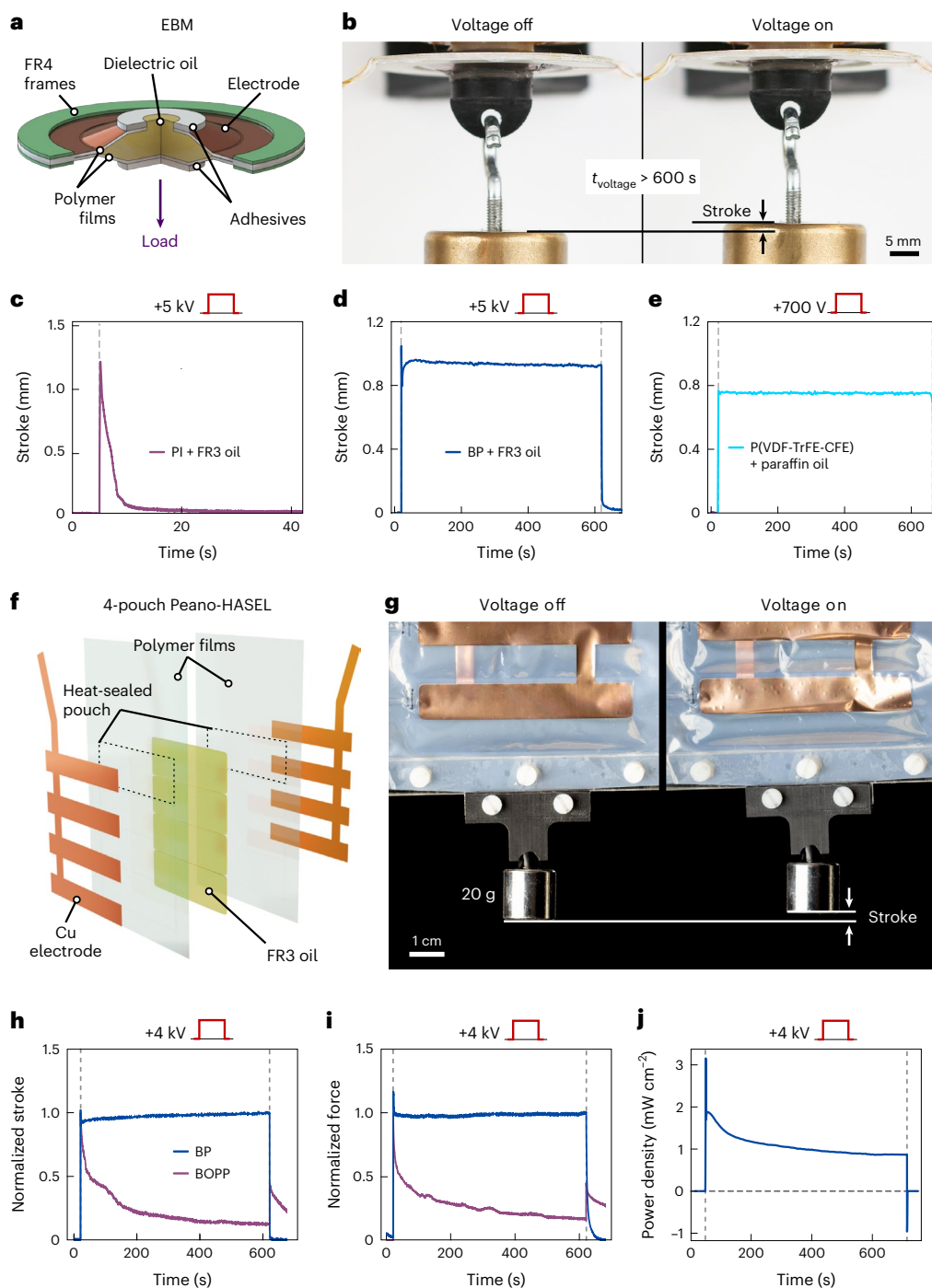


Fig. 4 | EBM and Peano-HASEL artificial muscles. a, Schematic of an EBM pouch during zipping. The zipping of the polymer films under high voltage evacuates the dielectric oil through a central opening and displaces the load. **b**, Photographs of a single-pouch EBM with a suspended mass. Left: the high voltage is off, and the load is fully extending the EBM. Right: high-voltage activation causes the EBM to pull the weight up and hold it for a time interval t_{voltage} of at least 600 s. **c**, Stroke for single-pouch EBM with PI and FR3 oil under 1 N load. The stroke experiences a 95% decay in less than 5 s. **d**, Single-pouch EBM with BP and FR3 oil subject to a 5 kV pulse and stressed by a 1 N constant load maintains its stroke over 600 s with minimal decay. **e**, Single-pouch EBM with P(VDF-TrFE-CFE) and paraffin oil subject to a 700 V pulse and stressed by a 0.1 N constant load maintains its stroke over 600 s without decay. **f**, Schematic of a

four-pouch Peano-HASEL consisting of three different materials, namely, Cu electrodes, polymer dielectric film and FR3 oil as a dielectric liquid. **g**, Peano-HASEL with BP dielectric films during steady-state actuation holding a 20 g suspended mass (actuation like that in **b**). **h**, Constant and decaying normalized stroke of two Peano-HASEL actuators under the constant-force condition (0.55 N) and subjected to a 4 kV high-voltage pulse for 600 s, made from BP or 19- μm -thick BOPP dielectric films, respectively. **i**, Normalized forces under the blocking condition for two Peano-HASEL actuators, same as in **g**, subjected to a 4 kV high-voltage pulse for 600 s. **j**, Power consumption of a fully zipped four-pouch Peano-HASEL actuator, made from BP, subjected to a 4 kV high-voltage pulse, normalized by the electrode surface.

per area, considering the larger thickness and lower permittivity of PI, as well as comparable finite remnant paraffin oil layers in both cases (Supplementary Equations (46) and (47)).

The Peano-HASEL actuator functions by zipping an electrode-covered portion of a pouch, pressurizing the encapsulated dielectric liquid. This deforms its soft pouches, thereby shortening the overall muscle length (Fig. 4f,g). A Peano-HASEL, fabricated with BOPP films with a heat-sealing layer (Supplementary Table 3), lost 50% stroke in the first 35 s, whereas if fabricated with BP films instead, it held a nearly constant stroke for 600 s (Fig. 4h). Additionally, we compared these two Peano-HASEL versions in terms of a blocking force exerted against a fixed load cell (Supplementary Fig. 12). We observed the same trends of decaying or maintaining a constant force for actuators made of BOPP or BP, respectively (Fig. 4i).

We then analysed the power loss density of the Peano-HASEL actuator incorporating BP by applying a 4 kV d.c. pulse for ~600 s. The measured power loss density decreases from an initial value of -2 mW cm^{-2} to -1 mW cm^{-2} (Fig. 4j), which is in accordance with the time dependency presented earlier.

Finally, we integrated Peano-HASEL actuators into lever arms, each holding a weight of 10 g (Fig. 1d, Supplementary Fig. 13 and Supplementary Video 5). On activation, both arms similarly displaced the weight. However, over the course of 300 s, the BOPP muscle lowered it down, whereas the BP one held the weight.

Conclusions

We have reported a theoretical and experimental framework to analyse and predict the force dynamics of EMSs. Our model describes a response to high-voltage signals for arbitrary stacks of dielectrics, which is largely determined by the permittivities and conductivities of the materials. These insights were then used to develop a material recipe to prevent charge accumulation at dielectric interfaces using lossy polymer films (BP and P(VDF-TrFE-CFE)) and achieve continuous quasistatic actuation in EMSs. Using our materials-screening technique, we investigated the force dynamics of commonly used dielectrics, suggested new material combinations and found good agreement between theoretical predictions based on dielectric parameters and experimental results. With a d.c. supply, our new material combinations cut power losses 100-fold (BP-FR3 oil) and up to 1,000-fold (P(VDF-TrFE-CFE)-paraffin oil) compared with conventional dielectrics. Furthermore, the latter allows a reduction in the driving voltages to 700 V. Enabled by such matched dielectrics, we demonstrated a steady force output for a range of EMSs driven by d.c. high voltages, including tunable lenses, haptic devices and artificial muscles. Our approach could be used to develop EMS-based transducers with energy and power efficiencies beyond conventional technologies. Key future challenges include further loss reduction via more insulating matched film and liquid-dielectric pairs and device miniaturization.

Methods

Polymer films

The force variation analysis (denominated as force measurements) employed five polymer films:

- PI-Linqtape PITIN (CAPLINQ), 25 μm thick;
- Uniaxially oriented PVDF (PolyK Technologies), 26 μm thick;
- PET (Hueck Folien), 25 μm thick;
- BOPP, 26 μm thick;
- BP (NATURAPACKAGING, Naturabiomat), 33 μm thick;
- P(VDF-TrFE-CFE) (PolyK Technologies), 8 μm thick.

Supplementary Table 1 provides the permittivity ϵ_f and conductivity σ_f values of these films. The permittivity is determined via dielectric spectroscopy, whereas the conductivity is measured in a custom high-voltage conductivity measurement setup.

The combinations of BP-FR3 oil, PET-FR3 oil and P(VDF-TrFE-CFE)-paraffin oil (as shown below) are employed in the power loss measurements to determine the losses associated with a.c. driving (PET-FR3 oil) and d.c. driving (BP-FR3 oil and P(VDF-TrFE-CFE)-paraffin oil).

The demonstrators featured five polymer materials:

- BP in the matched dielectrics versions of all actuators;
- P(VDF-TrFE-CFE) in the matched dielectrics version of the EBM;
- PI in the EBM;
- 19- μm -thick BOPP (Saropack) films with heat-sealing layers, in the Peano-HASEL actuators;
- 12- μm -thick PET films in the ZEAP lens.

Supplementary Table 3 presents all the dielectric materials of the demonstrators.

Dielectric liquids

The dielectric liquids employed in this work are as follows:

- Ester oil: Envirotemp FR3 (Cargill);
- Paraffin oil (Carl Roth).

Supplementary Table 2 lists their dielectric properties.

Electrodes

In this work, five types of electrode are used:

- (1) Metal electrodes. In a Univex 350 (Leybold) coating system, two metal layers are applied on one of the film's sides: a 3-nm-thick chromium adhesion layer, followed by a 150-nm-thick copper (Cu) electrode.
- (2) Carbon elastomeric paint. DAG-T-502 Carbon Paint (Ted Pella).
- (3) Carbon conductive tape, double coated (Ted Pella).
- (4) Carbon grease. Produced by mixing together ELBESIL B50 silicon oil and carbon black powder from ABCR, with an average particle size of 0.42 μm .
- (5) Conductive epoxy glue. Silver epoxy (MG Chemicals).

The custom shapes of the electrodes are either obtained by applying masks, laser-ablating the negative (Speedy 300 flexx, Trotec Laser) or mechanical cutting (conductive tape).

In the force measurements, BP has metallized electrodes because it is incompatible with the acetone solvent (carbon paint), PVDF is painted because it is sensitive to high temperatures (metal deposition) and P(VDF-TrFE-CFE) has silver epoxy electrodes because it is sensitive to high temperatures and various solvents. Electrodes on PI, PVDF, PET and BOPP are painted due to the simplicity of the process.

The EBM with a PI dielectric has painted electrodes, whereas both versions of Peano-HASEL, ZEAP lens and HAXEL, as well as the lossy BP version of the EBM, have metal electrodes. The EBM incorporating P(VDF-TrFE-CFE) films uses a conductive tape.

High-voltage generation

High voltage was achieved with a Trek 610D amplifier or a Trek 10/10B-HS amplifier, the latter being employed only for the EBM demonstrator.

The high-voltage dielectric spectroscopy experiments were performed with a Novocontrol Alpha A impedance analyser in combination with an HVB 1000 test interface (Novocontrol Technologies). The permittivity measurements of all of the polymer films, dielectric liquids and power loss measurements on PET-FR3 oil stacks are conducted in the frequency range between 50 and 200 Hz at test voltages up to 353 V_{r.m.s.}

Force measurement test bench

We employ a custom optomechanical setup (Supplementary Fig. 3a) to characterize the force variations in multilayer dielectric stacks with the same layout as an EMS, that is, electrode-polymer film-insulating

liquid–polymer film–electrode. Supplementary Fig. 3a shows the full assembly of the optomechanical setup using the following components:

- Cantilever. A $30.0 \times 8.0 \times 1.4 \text{ mm}^3$ rectangular beam of brass (Young's modulus of 102.3 GPa). The tail of the cantilever is fixed to a thick stainless steel support with a spherical-ball-shaped end. The spherical ball allows a parallel alignment of the cantilever with the static polymer film.
- Cantilever mirror. A rectangular $8 \times 10 \text{ mm}^2$ sheet of a 1-mm-thin glass coated with 100 nm of Cu on the back side. The mirror is placed close to the tip of the cantilever and is angled at 45° relative to the cantilever. The horizontal distance from the tip of the cantilever to the centre of the mirror is around 4 mm, which corresponds to half the length of the electrode attached to the cantilever.
- Micrometric stage. It is used to adjust the gap between the two polymer films.
- Laser. A helium–neon gas laser with a wavelength of 633 nm (red light) and power of 0.8 mW (Linos).
- Photodiode. PDP90A two-dimensional lateral effect position sensor (Thorlabs). It is used to detect the vertical displacement of the laser beam. The distance between the position sensor and mirror on the cantilever is $\sim 40 \text{ cm}$. This distance is sufficient to detect cantilever displacements in the order of 10^{-7} m .
- Other components. A circular-adjustable neutral-density filter (NDC-50C-2, Thorlabs), mirrors (PF10-03, Thorlabs), Thorlabs posts, brackets, mounts, tubes for the optical components and a stiff steel breadboard onto which everything is fixed.

Data acquisition and signal generation are performed with an NI USB-6351 multifunction input/output device at a sampling rate of 1 kHz, connected to a Windows personal computer, running NI LabVIEW 2018 SP1 (Supplementary Fig. 3b). The voltage signal is generated with the NI device and then amplified.

During the experiments, the setup is shielded from external interfering factors, such as high luminance variations, temperature change, air currents or mechanical vibrations.

Force measurement setup calibration

For the calibration of the setup, a known force is applied to the tip of the flexible cantilever, whereas the voltage signal is acquired from the photodiode; a linear regression function is then derived, which relates the photodiode voltage to the applied force. The latter is measured with a calibrated beam-type load cell (KD60 5 N, ME-Meßsysteme), connected on one end to the tip of the cantilever via a polyamide thread (diameter, 0.35 mm; Emil Lux) (Supplementary Fig. 3c) and on the other end, to a vertical micrometric stage.

Both photodiode and load-cell signals are acquired at a sampling rate of 1 kHz with the NI USB-6351 board running LabVIEW 2018 SP1 during seven stress cycles that slowly bend and release the cantilever.

Assembly of the cantilever dielectric stack

Supplementary Fig. 4 presents the process of assembling the dielectric stack. At first, small rectangular electrodes with an area of either $8 \times 8 \text{ mm}^2$ (cantilever electrode) or $8 \times 10 \text{ mm}^2$ (fixed electrode) (Supplementary Fig. 4a,b) are deposited on the polymer films. The film bearing the negative electrode is electrically connected to the grounded cantilever with carbon paint and Cu tape and glued with UHU Plus 2k epoxy glue such that the corners of the electrode correspond to the corners of the cantilever tip (Supplementary Fig. 4c,d).

The film with the high-voltage electrode is squeezed between two polymethyl methacrylate (PMMA) plates (3 mm thick). The bottom plate that faces the electrode side of the film is rigidly connected to the setup and has the role of a stiff support. The top plate faces the clear side of the film; it has a gap above the electrode, slightly larger than

the latter, so as to create an empty volume on the polymer surface. The cantilever is situated on the top of this gap and encloses it from above, whereas the empty volume serves as a bath where the oil is inserted. Supplementary Fig. 4f,g depicts this system, without the oil.

Force measurement experiments

The force characterization of the polymer film–dielectric liquid multilayer stacks is realized by measuring the response of the cantilever to two types of stimulus:

- 600-s-long pulse with unipolar high-voltage magnitudes of 4, 6 and 8 kV (Fig. 2b and Extended Data Fig. 6). This corresponds to half the period of a square wave with $T = 1,200 \text{ s}$ (for example, Extended Data Fig. 3 shows the 600 s pulse as half a square wave for comparative reasons).
- Square-wave high-voltage signals with periods (T) of 2 s (Extended Data Fig. 1), 20 s or 120 s (Extended Data Fig. 3) and an amplitude of 8 kV. These experiments have the same total duration as the unipolar excitations (600 s).

Additionally, we test the repeatability of the results with BP–FR3 oil by applying +8 kV d.c. high-voltage pulses for 600 s in consecutive tests (two times in the beginning and two times after 24 h) using the same sample (Extended Data Fig. 7).

High-voltage conductivity measurements

Polymer films. The conductivities of PET, BOPP, PVDF, PI, BP and P(VDF-TrFE-CFE) are measured with the setup shown in Supplementary Fig. 5. A square-shaped polymer sheet of $7 \times 7 \text{ cm}^2$ ($2 \times 2 \text{ cm}^2$ for P(VDF-TrFE-CFE)) is clamped by an aluminium frame and placed inside a shielded enclosure. This frame collects the leaking surface current, and it is connected via the shielded enclosure to the common ground. A direct current is passed through the polymer sheet via two square-shaped electrodes with an area of $2 \times 2 \text{ cm}^2$ (1.2 cm diameter, circular shaped for P(VDF-TrFE-CFE)). The hot electrode was connected to high-voltage capacitors with a total capacitance of $C_{\text{HV}} = 33 \mu\text{F}$. The capacitors are initially charged to a potential of $U_{\text{HV}} \leq 1 \text{ kV}$ via an external contact and provide a smooth, noise-free high-voltage potential. This potential is then measured contact free by a Kelvin probe of an electrostatic voltmeter (ISOPROBE 244, Monroe Electronics). The current through the polymer sheet is measured with a Keithley 6514 electrometer, where a current-limiting high-voltage resistor with $R_L = 10 \text{ M}\Omega$ restricts the maximum current to 100 μA in the case of a breakdown event. The conductivity values are calculated from the obtained data after more than 36 h when the polarization current has reduced below the hopping current.

Dielectric liquid. A cylinder capacitor arrangement of two concentric Cu tubes is used as the test cell for d.c. high-voltage conductivity measurements. With an outer diameter of 18 mm for the inner tube and an inner diameter of 20 mm for the outer tube, the dielectric liquids fill a 1 mm gap over an effective electrode length of 100 mm. The outer Cu tube is grounded, whereas the inner tube is connected to a high voltage. The direct current is measured with a Keithley 6514 electrometer. Five consecutive voltage steps (1, 3, 5, 7 and 8 kV) are applied to the dielectric liquid for 6 h each as the leakage current is continuously monitored.

Dielectric spectroscopy to determine permittivities

Polymer films. The polymer films are provided with $5 \times 5 \text{ cm}^2$ Cu (1.2 cm diameter, circular shaped for P(VDF-TrFE-CFE)) electrodes on both sides, fixed inside a metal box and electrically connected via high-voltage BNC connectors to the impedance analyser.

Dielectric liquid. A parallel-plate capacitor arrangement of two planar Cu discs (17 mm thick and 100 mm diameter) is used as a test cell for a.c. conductivity measurements. A parallel gap of 100 μm between

the horizontally levelled Cu discs is created with three $4 \times 4 \text{ mm}^2$ small polytetrafluoroethylene foils. The gap between the discs was filled with the dielectric liquid under test by the action of capillary force. The liquid is prevented from outflow by a $25\text{-}\mu\text{m}$ -thin foil of polypropylene that encloses the lower Cu disc and opens dish-shaped upwards across the gap. The entire arrangement was placed in a closed metal box and electrically connected via high-voltage BNC connectors to our impedance analyser.

Hysteresis measurement

Hysteresis measurements were performed with a Sawyer–Tower circuit (Supplementary Fig. 6). A triangular-wave signal of 20 Hz was used and amplified with a Trek PD05034 high-voltage amplifier. Data acquisition was accomplished with a LeCroy Waverunner oscilloscope.

Sample electrodes of 12 mm diameter were shadow-mask painted with the conductive carbon grease paint.

Power loss measurement

Power loss (d.c.). The electrical d.c.-power dissipation of a BP–FR3 oil and a P(VDF-TrFE-CFE)–paraffin oil stack system is measured with the system shown in Supplementary Fig. 8. The BP–FR3 oil stack holds rectangular Cu electrodes with an area of $2 \times 2 \text{ cm}^2$ and the P(VDF-TrFE-CFE)–paraffin oil stack holds a circular carbon grease electrode with a diameter of 1.2 cm on its external surfaces. The sample is clamped and held in place by a square-shaped PMMA frame. The top inner volume of the frame is filled with FR3 oil to avoid corona discharge currents at the high-voltage electrode contact. The direct current is measured with a Keithley 6514 electrometer. Four consecutive voltage steps (1, 3, 5 and 7 kV) are applied for 24 h (BP–FR3 oil) or 6 h (P(VDF-TrFE-CFE)–paraffin oil) each as the leakage current is continuously monitored (Extended Data Fig. 9).

Power loss (a.c.). The a.c. power loss tests are performed on PET–FR3 oil stacks. These stacks are provided with rectangular Cu electrodes of $2 \times 2 \text{ cm}^2$ and fixed with a square-shaped PMMA frame (Supplementary Fig. 8). The frame is placed inside a metal box with high-voltage BNC connectors to which the electrodes are connected.

The a.c. power loss is calculated from the values of the dielectric loss factor $\tan\delta$ and the real part C' of the stack capacitance. These values are acquired from dielectric spectroscopy measurements performed on the stack. The power loss corresponding to 1, 3, 5 and 7 kV is estimated via the extrapolation of the dielectric spectroscopy results obtained at $353 \text{ V}_{\text{r.m.s.}}$.

Demonstrators

Demonstrators are made of single or multiple (Peano-HASEL) dielectric pouches (dielectric stacks in which the oil is sealed), holding electrodes on external surfaces. Pouches incorporating BP and BOPP as the dielectric films are created by thermal welding. In the case of EBM, the BP films are temporarily sandwiched between two protective PI films and pressed in a custom heat press (Supplementary Fig. 11b). The dies of the press have a flat annular shape and create a circular bonding distanced 1 mm from the electrodes. The other actuators use the same heat-sealing procedure as described in a previous publication³¹. In contrast, EBM pouches using PI (thermoset material) and P(VDF-TrFE-CFE) as dielectric films are created by attaching two films together with a $5\text{-}\mu\text{m}$ -thick double-sided adhesive (no. 5600, Nitto Denko) (Supplementary Fig. 11c). Similarly, the PET foils of the ZEAP lenses are bonded using a 3M VHB 467MP adhesive tape.

The filling of the EBM is done through its central opening. All the other actuators employ a silicone tube glued into the unwelded channels with silicone glue (Elastosil E4, Wacker Chemie).

ZEAP lens. The design and fabrication procedure for the ZEAP lens are based on a previous publication³¹ and presented in Supplementary Fig. 9.

The fabrication procedure was adapted with respect to the following steps: polymer films are glued to PDMS (SYLGARD 184, Dow Corning) parts and the PDMS parts are glued to each other using silicone glue. Once the lens itself is assembled, a small 1-mm-thick PMMA plate is glued under the PDMS base with silicone glue to increase the stiffness of the device. The resulting ZEAP lens has an overall diameter of 20 mm, from which 6 mm is the diameter of the concentric elastic membrane (Supplementary Fig. 9b).

To determine the response of the lens, it is placed in front of a basin of water-diluted rhodamine 6G, whereas a laser beam—slightly offset to the optical axis—is directed through the lens (Supplementary Fig. 9c). An amplified step-voltage function, generated by a Raspberry PI 4 microcomputer with a high-precision AD/DA expansion board (Waveshare Electronics) was used to drive the lens. During actuation, the deflection of the beam is recorded with a camera in the top view. Image recognition (Mathematica, Wolfram Research) is used to track the position of the laser spot at an image plane at the end of the basin (Supplementary Fig. 9d,e). The relative position change can, thus, be determined, which, in turn, is proportional to the relative focal length change³¹. We tested the lenses incorporating either PET or BP with d.c. high voltage at 1.5 kV for 300 s.

HAXEL. In our HAXELs, the PDMS membranes serve as haptic pixels able to provide tactile feedback (Supplementary Fig. 10a). The perimeter of the pouch welding is determined by the actuator's square shape ($6 \times 6 \text{ mm}^2$) (Supplementary Fig. 10b). After thermal welding, the top surface is glued with silicone glue to a $100\text{-}\mu\text{m}$ -thick uniform PDMS sheet, which is created by blade casting (ZUA 2000.200, Zehntner). The bottom side of the pouch is glued to a $100\text{-}\mu\text{m}$ -thick PI film that serves as a flexible substrate. Last, the device is filled with paraffin oil. The small amount of liquid needed is difficult to determine. Thus, the filling is chosen such that the device completely zips under 3 kV high-voltage application.

The force generated by the HAXEL is measured with the force sensor of a tensile tester (Xforce HP 100 N & Z005, ZwickRoell). The HAXEL is attached with an adhesive (VHB 467MP, 3M) to a flat metal table (Supplementary Fig. 10c). A small cylindrical pin attached to the force sensor of the tensile tester is positioned so as to touch the HAXEL membrane and apply a small preload of about 10 mN on it. The position of the pin is kept constant during the experiment duration. High voltage is provided in a similar manner with the ZEAP lens.

We performed two tests with the device: first, it is subjected to 3 kV d.c. for 600 s and second, the voltage is increased stepwise from 2 to 4 kV in 1 kV steps—each step is held for 250 s and then decreased back to 2 kV afterwards in the same manner.

EBM. The design and fabrication procedure of an EBM is based on a previous publication²⁹ and is presented in Fig. 4 and Supplementary Fig. 11a. Here, however, we used FR3 oil to fill the EBM pouches made of BP and paraffin oil for the P(VDF-TrFE-CFE) pouches. Two EBM prototypes with PI dielectrics used both oils, in accordance with the steady-state EBM that they are compared with. All the prototypes bear concentric annular frames made of FR-4 epoxy resin (0.5 mm thick), attached to the pouch with double-sided adhesive tape (Axton), one frame on each side so as to enclose the polymer films and cover the bonding regions of the pouch.

The P(VDF-TrFE-CFE) films have very poor mechanical strength due to their low thickness; consequently, a pouch with this dielectric must be mechanically enhanced by additional structural components. This was done by attaching two PI films to the external sides of the double-coated adhesive electrodes. As a result, each electrode holds a P(VDF-TrFE-CFE) film on the dielectric side and a structural PI layer on the other side. The electrodes together with the PI structural layers run over the entire diameter of the device and are clamped by the frames.

In the case of BP EBM and its PI counterpart, the reservoir and the end effector (for connecting the load) are attached to the pouch using a 1.0-mm-thick layer of silicone glue. In the P(VDF-TrFE-CFE) EBM and its corresponding PI version, these are attached with 0.5-mm-thick 3M VHB 4905 double-sided adhesive tape.

The EBM is mechanically loaded using a tensioned PDMS band attached to a load cell (RB-Phi-118, 780 g). The stroke of the actuator is measured with a laser displacement sensor (LK-G 152, Keyence), positioned below the EBM. This setup is a variation of the test bench presented in another work²⁹ and is shown in Supplementary Fig. 12a,b.

High voltage is applied to the actuator using an amplifier, driven by a Speedgoat baseline control and acquisition computer. To evaluate the behaviour of the three prototypes, a 600-s-long high-voltage pulse is applied to the BP (5 kV) and P(VDF-TrFE-CFE) (700 V) EBM and only a 60-s-long pulse to the PI EBM (considering the fast force decay).

Peano-HASEL. Functionality of Peano-HASEL actuators is analogous to other reported devices. Four-pouch actuators are built and presented. The pouches have 20.0 × 60.5 mm² rectangular surfaces, with the electrodes covering only the top halves (electrode surface, 10.0 × 60.0 mm²). Each pouch is filled with 1.2 ml of FR3 oil. Two-mm-thick PMMA clamps are attached to the Peano-HASEL with VHB adhesive tape and plastic screws. The actuator is mounted in the setup shown in Supplementary Fig. 12a.

NI LabView program acquires the data of the laser distance sensor (HG-C103, Panasonic) and the force sensor (KD60 5 N, ME-Meßsysteme) via a data acquisition device (USB X Series, NI) and is used to control the output voltage of the amplifier.

The stroke of the Peano-HASEL actuators is characterized in constant-force conditions (Supplementary Fig. 12b). They are subjected to a load of 0.55 N and their displacement is measured at a high-voltage excitation of +4 kV.

For the force characterization, the end effector is blocked (fixed stroke) by establishing a rigid connection between the actuator and force sensor using an M4 screw (Supplementary Fig. 12c). We applied a small preload of <0.2 N in the unzipped state and subjected the actuators to +4 kV for 600 s.

The power loss of the Peano-HASEL made of BP dielectric films is estimated from the leakage current measurements. The current is measured in a similar fashion to the conductivity measurements of the individual polymer films, described earlier, by employing a Keithley 6514 electrometer and a current-limiting resistor (Supplementary Fig. 5). During this experiment, no load is applied to the actuator; therefore, as the device is subjected to a high voltage of +4 kV, the electrodes of the actuator are almost completely zipped. The power consumption is normalized to the electrode area.

Peano-HASEL lever arms. We integrated four-pouch Peano-HASEL actuators in a lever resembling an artificial arm, made of 3.5-mm-thick light plywood (Supplementary Fig. 13). The latter has a 10 g suspended mass attached to its extremity. We employ Peano-HASEL actuators incorporating either BP or BOPP as the polymer dielectric in this demonstration and apply 4 kV unipolar voltage to both actuators for 300 s.

Data availability

The data that support the plots within this paper and other findings of this study are available from the corresponding authors on reasonable request.

References

- Rus, D. & Tolley, M. T. Design, fabrication and control of soft robots. *Nature* **521**, 467–475 (2015).
- Rothmund, P. et al. Shaping the future of robotics through materials innovation. *Nat. Mater.* **20**, 1582–1587 (2021).
- Whitesides, G. M. Soft robotics. *Angew. Chem. Int. Ed.* **57**, 4258–4273 (2018).
- Polygerinos, P. et al. Soft robotics: review of fluid-driven intrinsically soft devices; manufacturing, sensing, control, and applications in human-robot interaction. *Adv. Eng. Mater.* **19**, 1700016 (2017).
- Cianchetti, M., Laschi, C., Menciassi, A. & Dario, P. Biomedical applications of soft robotics. *Nat. Rev. Mater.* **3**, 143–153 (2018).
- El-Atab, N. et al. Soft actuators for soft robotic applications: a review. *Adv. Intell. Syst.* **2**, 2000128 (2020).
- Li, M., Pal, A., Aghakhani, A., Pena-Francesch, A. & Sitti, M. Soft actuators for real-world applications. *Nat. Rev. Mater.* **7**, 235–249 (2022).
- Rich, S. I., Wood, R. J. & Majidi, C. Untethered soft robotics. *Nat. Electron.* **1**, 102–112 (2018).
- Ilami, M., Bagheri, H., Ahmed, R., Skowronek, E. O. & Marvi, H. Materials, actuators, and sensors for soft bioinspired robots. *Adv. Mater.* **33**, e2003139 (2021).
- Heiden, A. et al. 3D printing of resilient biogels for omnidirectional and exteroceptive soft actuators. *Sci. Robot.* **7**, eabk2119 (2022).
- Wehner, M. et al. An integrated design and fabrication strategy for entirely soft, autonomous robots. *Nature* **536**, 451–455 (2016).
- Yang, T. H., Shintake, J., Kanno, R., Kao, C. R. & Mizuno, J. Low-cost sensor-rich fluidic elastomer actuators embedded with paper electronics. *Adv. Intell. Syst.* **2**, 2000025 (2020).
- Lendlein, A. & Gould, O. E. C. Reprogrammable recovery and actuation behaviour of shape-memory polymers. *Nat. Rev. Mater.* **4**, 116–133 (2019).
- Chen, C. & Yi, Z. G. Photostrictive effect: characterization techniques, materials, and applications. *Adv. Funct. Mater.* **31**, 2010706 (2021).
- Sitti, M. & Wiersma, D. S. Pros and cons: magnetic versus optical microrobots. *Adv. Mater.* **32**, e1906766 (2020).
- Mao, G. Y. et al. Ultrafast small-scale soft electromagnetic robots. *Nat. Commun.* **13**, 4456 (2022).
- Bar-Cohen, Y. (ed.) in *Electroactive Polymer (EAP) Actuators as Artificial Muscles: Reality, Potential, and Challenges* 3–50 (SPIE, 2004).
- Haines, C. S. et al. Artificial muscles from fishing line and sewing thread. *Science* **343**, 868–872 (2014).
- Haines, C. S. et al. New twist on artificial muscles. *Proc. Natl Acad. Sci. USA* **113**, 11709–11716 (2016).
- Liu, C., Qin, H. & Mather, P. T. Review of progress in shape-memory polymers. *J. Mater. Chem.* **17**, 1543–1558 (2007).
- Bluett, S., Helps, T., Taghavi, M. & Rossiter, J. Self-sensing electro-ribbon actuators. *IEEE Robot. Autom. Lett.* **5**, 3931–3936 (2020).
- Ly, K. et al. Miniaturized circuitry for capacitive self-sensing and closed-loop control of soft electrostatic transducers. *Soft Robot.* **8**, 673–686 (2021).
- Rothmund, P., Kellaris, N., Mitchell, S. K., Acome, E. & Keplinger, C. HASEL artificial muscles for a new generation of lifelike robots—recent progress and future opportunities. *Adv. Mater.* **33**, 2003375 (2021).
- Moretti, G., Duranti, M., Righi, M., Vertechy, R. & Fontana, M. Analysis of dielectric fluid transducers. In *Proc. SPIE 10594, Electroactive Polymer Actuators and Devices (EAPAD) XX* (ed. Bar-Cohen, Y) 105940W (SPIE, 2018).
- Acome, E. et al. Hydraulically amplified self-healing electrostatic actuators with muscle-like performance. *Science* **359**, 61–65 (2018).
- Kellaris, N., Venkata, V. G., Smith, G. M., Mitchell, S. K. & Keplinger, C. Peano-HASEL actuators: muscle-mimetic, electrohydraulic transducers that linearly contract on activation. *Sci. Robot.* **3**, eaar3276 (2018).

27. Taghavi, M., Helps, T. & Rossiter, J. Electro-ribbon actuators and electro-origami robots. *Sci. Robot.* **3**, eaar3276 (2018).
28. Wang, X. R., Mitchell, S. K., Rumley, E. H., Rothmund, P. & Keplinger, C. High-strain Peano-HASEL actuators. *Adv. Funct. Mater.* **30**, 1908821 (2020).
29. Sirbu, I. D. et al. Electrostatic bellow muscle actuators and energy harvesters that stack up. *Sci. Robot.* **6**, eaaz5796 (2021).
30. Yoder, Z. et al. A soft, fast and versatile electrohydraulic gripper with capacitive object size detection. *Adv. Funct. Mater.* **33**, 2209080 (2022).
31. Hartmann, F., Penkner, L., Danninger, D., Arnold, N. & Kaltenbrunner, M. Soft tunable lenses based on zipping electroactive polymer actuators. *Adv. Sci.* **8**, 2003104 (2021).
32. Leroy, E., Hinchet, R. & Shea, H. Multimode hydraulically amplified electrostatic actuators for wearable haptics. *Adv. Mater.* **32**, e2002564 (2020).
33. Sirbu, I. D. et al. Electrostatic actuator for tactile display based on hydraulically coupled dielectric fluids and soft structures. *Electroact. Polym. Actuators Devices (EAPAD) XXI* **10966**, 334–339 (2019).
34. Han, A. K., Ji, S., Wang, D. X. & Cutkosky, M. R. R. Haptic surface display based on miniature dielectric fluid transducers. *IEEE Robot. Autom. Lett.* **5**, 4021–4027 (2020).
35. Helps, T., Romero, C., Taghavi, M., Conn, A. T. & Rossiter, J. Liquid-amplified zipping actuators for micro-air vehicles with transmission-free flapping. *Sci. Robot.* **7**, eabi8189 (2022).
36. Duranti, M., Righi, M., Vertechy, R. & Fontana, M. A new class of variable capacitance generators based on the dielectric fluid transducer. *Smart Mater. Struct.* **26**, 115014 (2017).
37. Iwamoto, M. in *Encyclopedia of Nanotechnology* (ed. Bhushan, B.) 1904–1915 (Springer, 2016).
38. Srinivasan, R. & Fasmin, F. *Introduction to Electrochemical Impedance Spectroscopy* 1st edn (CRC Press, 2021).
39. Lvovich, V. F. *Impedance Spectroscopy: Applications to Electrochemical and Dielectric Phenomena* (Wiley, 2012).
40. Kremer, F. & Schönhals, A. *Broadband Dielectric Spectroscopy* (Springer, 2003).
41. Brock, J. *Electrochemical Impedance Spectroscopy: Methods, Analysis, and Research* (Nova Science Publishers, 2017).
42. Barsoukov, E. & Macdonald, J. R. *Impedance Spectroscopy: Theory, Experiment, and Applications* 3rd edn (Wiley, 2018).
43. Prodromakis, T. & Papavassiliou, C. Engineering the Maxwell-Wagner polarization effect. *Appl. Surf. Sci.* **255**, 6989–6994 (2009).
44. Kellaris, N., Venkata, V. G., Rothmund, P. & Keplinger, C. An analytical model for the design of Peano-HASEL actuators with drastically improved performance. *Extreme Mech. Lett.* **29**, 100449 (2019).
45. Rothmund, P., Kirkman, S. & Keplinger, C. Dynamics of electrohydraulic soft actuators. *Proc. Natl Acad. Sci. USA* **117**, 16207–16213 (2020).
46. Bartnikas, R. *Electrical Insulating Liquids* (ASTM, 1994).
47. Tenbohlen, S. & Koch, M. Aging performance and moisture solubility of vegetable oils for power transformers. *IEEE Trans. Power Del.* **25**, 825–830 (2010).
48. Rumley, E. H. et al. Biodegradable electrohydraulic actuators for sustainable soft robots. *Sci. Adv.* **9**, eadf5551 (2023).

Acknowledgements

We thank NATURABIOMAT GmbH, especially Managing Director G. Margreiter, for fruitful discussions and providing NATURAPACKAGING (BP) films. M.K. acknowledges support from the European Research Council Starting Grant ‘Gel-Sys’ under grant agreement no. 757931

and support from the European Union’s Horizon 2020 research and innovation programme under grant agreement no. 101016411. I.-D.S., G.M. and M.F. acknowledge support from the Italian Ministry of Education, University and Research (MUR), under the Program Department of Excellence, awarded to the Department of Industrial Engineering of the University of Trento, Italy, and to the Department of Excellence of Robotics and AI of Scuola Superiore Sant’Anna, Italy. M.F. acknowledges support from the project ‘Sviluppo e valutazione socio-tecnico-economica-ambientale di nuove tecnologie basate su Materiali Multifunzionali per la conversione di Energia Rinnovabile’ under project nr. MAMER21MF, given by the ‘Programma Nazionale per la Ricerca (PNR)’ (DM no. 737/2021).

Author contributions

M.K., M.F., R.S. and G.M. formulated the goals of this research. M.K. and M.F. planned and coordinated the research activities. M.K., M.F., R.S. and N.A. supervised the work. N.A. and G.M. developed the analytical framework and the equivalent circuit models. R.S., I.-D.S., D.P. and L.P. designed the experiments and built most of the experimental test benches. I.-D.S. and R.S. performed the force measurements in dielectric stacks. R.S. and D.P. performed the high-voltage conductivity and power loss measurements. R.S., D.P. and I.-D.S. performed the dielectric spectroscopy measurements to determine the complex permittivities. L.P. and I.-D.S. fabricated and tested the demonstrators. I.-D.S., D.P. and R.S. curated the data. D.P., N.A., I.-D.S., R.S., L.P. and G.M. analysed and processed the experimental data. N.A., D.P., R.S., D.D. and G.M. validated the models. D.P., N.A., I.-D.S., D.D. and L.P. visualized the data. I.-D.S., N.A., D.P. and D.D. wrote the initial paper draft. All authors contributed to reviewing and editing and accepted the final paper.

Competing interests

The authors declare no competing interests.

Additional information

Extended data is available for this paper at <https://doi.org/10.1038/s41928-023-01057-0>.

Supplementary information The online version contains supplementary material available at <https://doi.org/10.1038/s41928-023-01057-0>.

Correspondence and requests for materials should be addressed to Marco Fontana or Martin Kaltenbrunner.

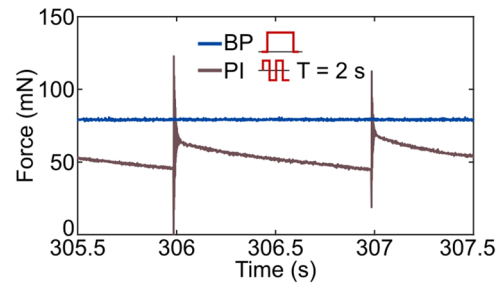
Peer review information *Nature Electronics* thanks the anonymous reviewers for their contribution to the peer review of this work.

Reprints and permissions information is available at www.nature.com/reprints.

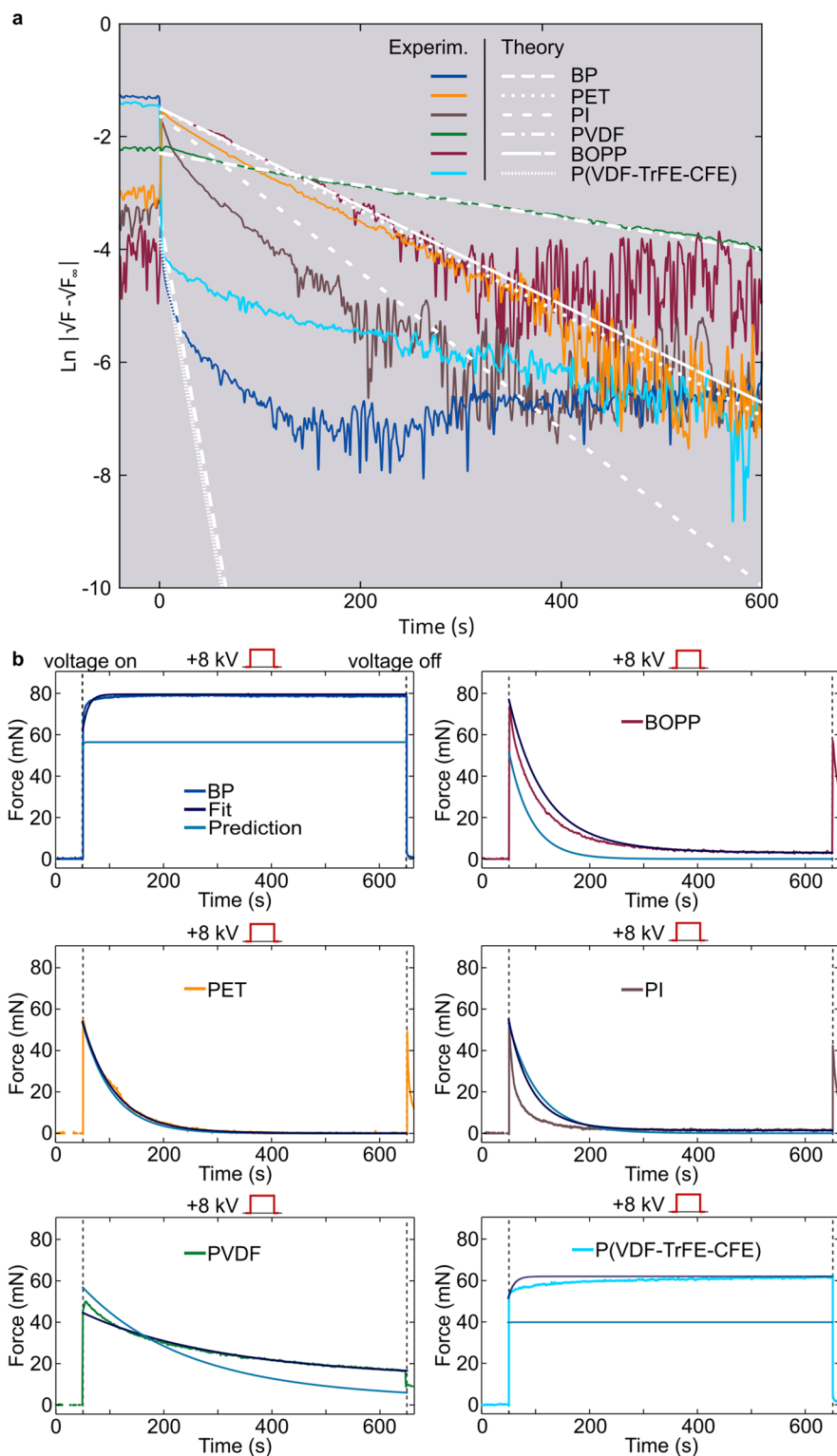
Publisher’s note Springer Nature remains neutral with regard to jurisdictional claims in published maps and institutional affiliations.

Springer Nature or its licensor (e.g. a society or other partner) holds exclusive rights to this article under a publishing agreement with the author(s) or other rightsholder(s); author self-archiving of the accepted manuscript version of this article is solely governed by the terms of such publishing agreement and applicable law.

© The Author(s), under exclusive licence to Springer Nature Limited 2023

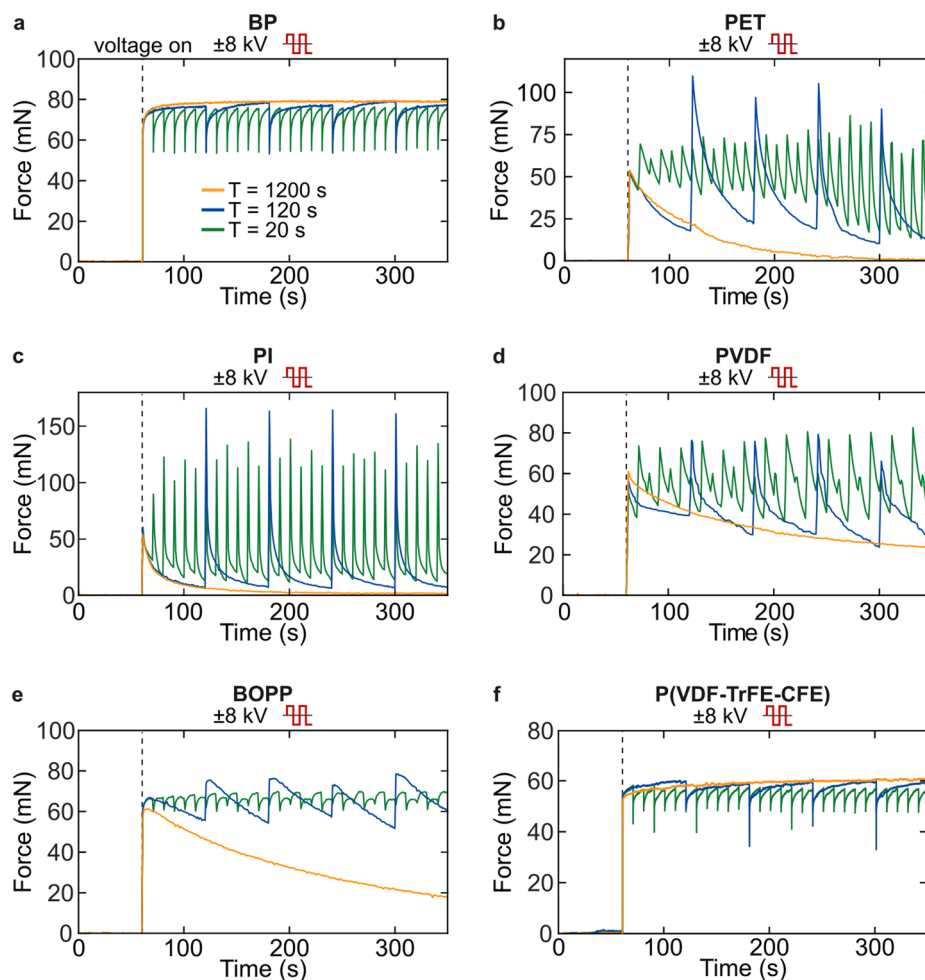


Extended Data Fig. 1 | Force response of two different multilayer stacks. Smooth constant force for a stack with BP under constant 8 kV and force spikes (recalculated from the opto-electronically recorded displacement using static calibration) at the moments of inversion (seconds 306 and 307) for PI-based dielectric stack under 8 kV square wave with 2 s period.

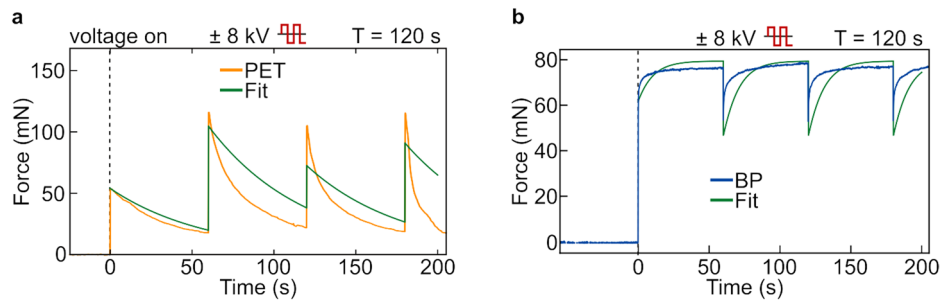


Extended Data Fig. 2 | Model validation. **a**, The decay of the electric field $E_L - E_{L,\infty} \propto \sqrt{F} - \sqrt{F_\infty}$ is close to a single-exponential for each dielectric material combination. All dielectric films are tested in combination with FR3 oil except P(VDF-TrFE-CFE) which is combined with paraffin oil. **b**, Fits of force responses for each tested material combination (films are color-coded in

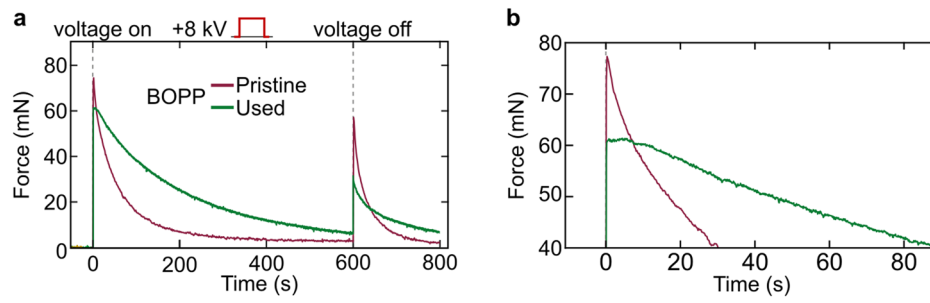
the 1st panel). The 'Fit' curves approximate the experimental data by optimizing the fitting parameters F_0 , F_∞ , and τ in Eq. (1), whereas the 'Prediction' curves use their theoretical values, independently calculated with the material parameters ϵ and σ from the dielectric spectroscopy and conductivity measurements.



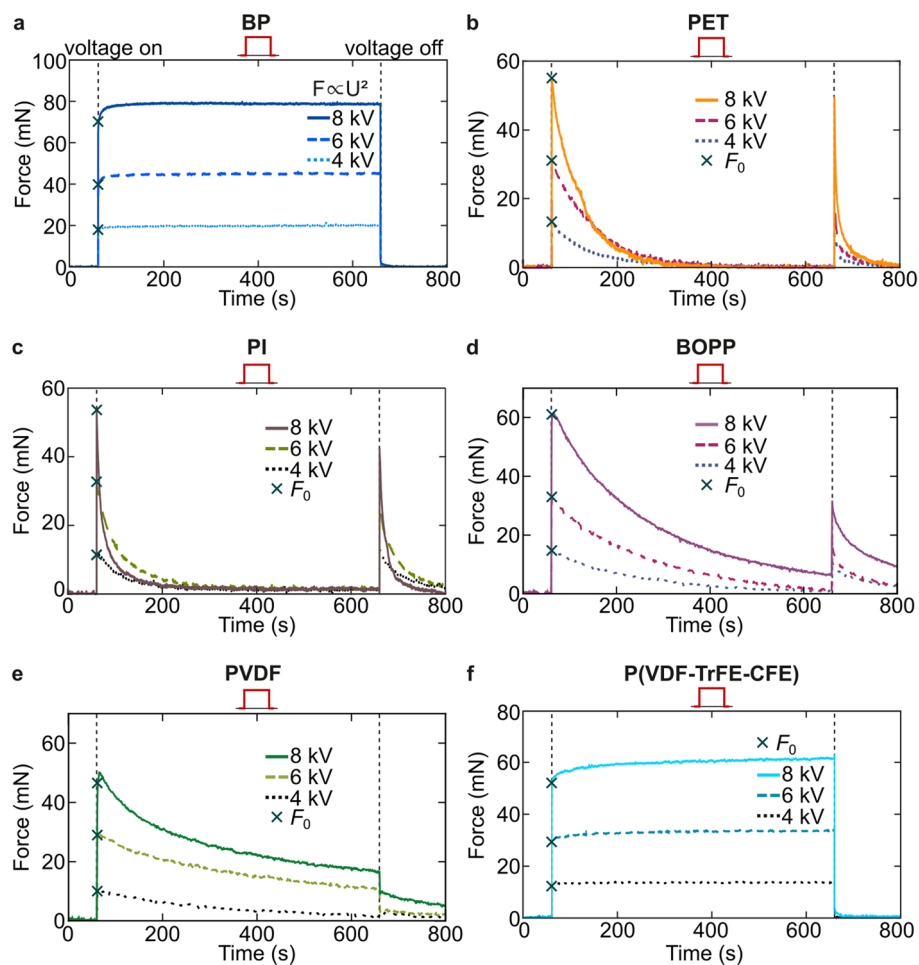
Extended Data Fig. 3 | Frequency dependence of force responses. a-f, Responses of BP, PET, PI, PVDF and BOPP film combined with FR3 oil as well as P(VDF-TrFE-CFE) combined with paraffin oil when driven with bipolar square wave high voltage of 8 kV and periods T of 20, 120, and 1200 s.



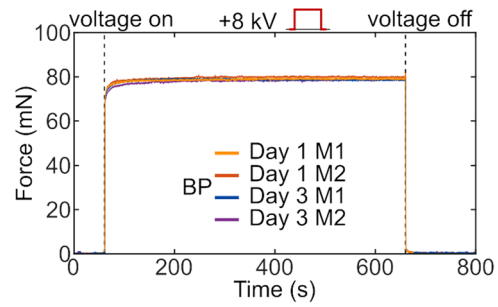
Extended Data Fig. 4 | Fitting of square wave high voltage response of multilayer stacks. a. Highly insulating film (PET). **b.** Lossy dielectric film (BP).



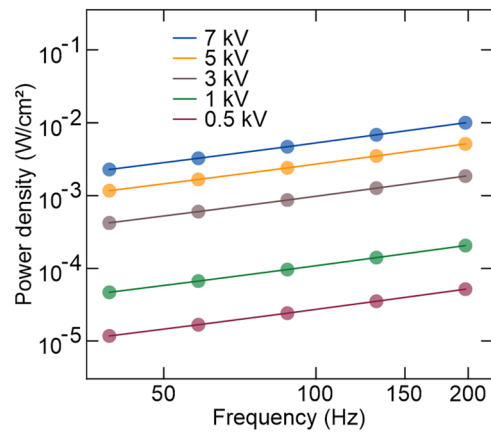
Extended Data Fig. 5 | Change of BOPP force response. It was first exposed to high voltage of +8 kV, shown **a**, for the entire duration (600 s) and **b**, zoomed in.



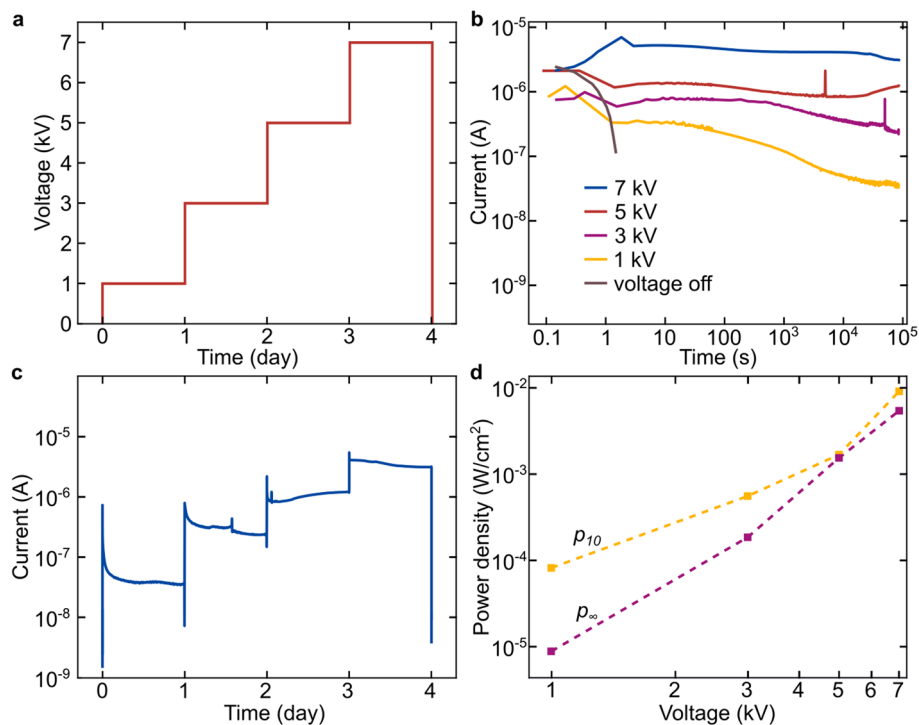
Extended Data Fig. 6 | Voltage dependent force responses of various dielectric film and oil combinations. a-f, Force response at unipolar constant voltages of 4, 6 and 8 kV applied for 600 s. All dielectric films are combined with FR3 oil, except P(VDF-TrFE-CFE) which is combined with paraffin oil.



Extended Data Fig. 7 | BP force repeatability at +8 kV. Experiments were performed consecutively (M1 and M2, respectively) or on different days. All curves were measured with the same sample.



Extended Data Fig. 8 | Power loss normalized to the electrode surface for a PET-FR3 oil stack as a function of frequency. The loss factor and the capacitance were measured by dielectric spectroscopy, subjecting the stack to a 0.5 kV sinusoidal signal in the frequency range 50–200 Hz, hence the power loss at 0.5 kV was calculated. For higher voltage amplitudes, the power loss was extrapolated from the 0.5 kV data.

**Extended Data Fig. 9 | Measured current through BP-FR3 oil stacks.**

Experiments were performed in the setup from Supplementary Fig. 8. **a**, The stacks were subject to four consecutive voltage steps of 1, 3, 5 and 7 kV, each with a duration of 1 day and constant magnitude. **b**, Measured current on a logarithmic

timescale for each voltage step. **c**, Measured current on a 4-day timeline. **d**, Power loss normalized to electrode surface at the beginning of each HV step (at 10 s) – yellow line, and after 24 h – purple line.